

Research Article www.acsami.org

# Progressive "Layer to Hybrid Spinel/Layer" Phase Evolution with Proton and Zn2+ Co-intercalation to Enable High Performance of MnO<sub>2</sub>-Based Aqueous Batteries

Shouxiang Ding, Lele Liu, Runzhi Qin, Xin Chen, Aoye Song, Jiawen Li, Shunning Li, Qinghe Zhao,\* and Feng Pan\*



Cite This: ACS Appl. Mater. Interfaces 2021, 13, 22466-22474



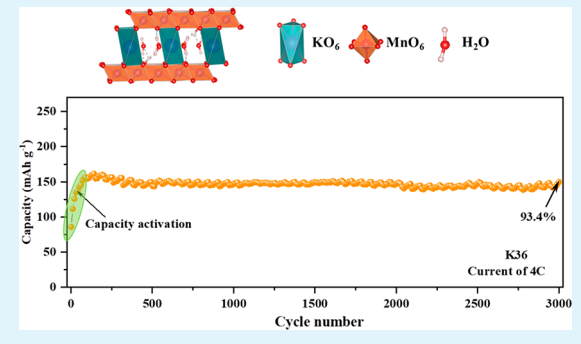
**ACCESS** 

III Metrics & More

Article Recommendations

Supporting Information

ABSTRACT: Manganese oxides are promising host materials in rechargeable aqueous batteries due to their low cost and high capacity; however, their practical applications have long been restricted by their sluggish reaction kinetics and poor cycling stability. Herein, the layered K<sub>0.36</sub>H<sub>0.26</sub>MnO<sub>2</sub>·0.28H<sub>2</sub>O (K36) with a proton and Zn<sup>2+</sup> cointercalation mechanism leads to a progressive phase evolution from layer-type K36 to hybrid layer-type K<sub>x</sub>H<sub>y</sub>Zn<sub>z</sub>MnO<sub>2</sub>·nH<sub>2</sub>O and spinel-type ZnMn<sub>2</sub>O<sub>4</sub> nanocrystal after a long-term cycle. Accordingly, K36 shows a high specific capacity (~329.8 mAh g<sup>-1</sup> at 0.1C), a superior rate performance (~100.1 mAh g<sup>-1</sup> at 10C), and a remarkable cycling stability (capacity retention of ~93.4% over 3000 cycles at 4C). This work provides a new viewpoint of enhancing electrode performance via generating hybrid phases under



electrochemical driving and will be a benefit to developing the next-generation aqueous batteries.

KEYWORDS: manganese oxide, phase evolution, aqueous batteries, intercalation mechanism, cycling stability

### 1. INTRODUCTION

The ever-increasing demand for advanced batteries for economical and sustainable energy storage has intensified attention from researchers all over the world, and rechargeable aqueous Zn-ion batteries (RAZBs) are among the best candidates of the next-generation batteries, mainly due to the advantages of low cost, environmental friendliness, high power density, and high ionic conductivity in aqueous electrolytes. For practical application of RAZBs in future, some issues in both the Zn anode (such as dendrite formation, side reactions, corrosion, etc.)<sup>1-5</sup> and the cathode materials (such as structural instability, sluggish Zn2+ diffusion kinetics, etc.) must be resolved. So far, several kinds of cathode materials, such as Mn-based oxides,6-Prussian blue analogues, 9,10 V-based oxides, 11,12 and organic compounds, 13,14 have been reported in RAZBs, among which the MnO<sub>2</sub> materials present the highest potential as cathode materials, based on a comprehensive consideration of high energy density and low manufacturing cost.

MnO<sub>2</sub> materials with various crystalline structures (such as  $\alpha$ -, <sup>15</sup>  $\beta$ -, <sup>16</sup>  $\gamma$ -, <sup>17</sup>  $\delta$ -, <sup>18</sup> spinel, <sup>19</sup> amorphous, <sup>20</sup> etc.) are electrochemically active in RAZBs. Among these materials, the layertype MnO<sub>2</sub> materials with a wide interlayer spacing ( $\sim$ 7.0 Å) have been proposed to be the most suitable host materials for facile H<sup>+</sup> and Zn<sup>2+</sup> intercalation/extraction. <sup>21,22</sup> Besides, it is reported that preintercalating water, ions, or molecules in the interlayer space of layered MnO2 plays a significant role in realizing superior electrode properties via enhancing intrinsic conductivity, activating reaction sites, promoting diffusion kinetics, stabilizing structural integrity, etc.<sup>23</sup> For instance, the layer-type  $\delta$ -MnO<sub>2</sub> stabilized by hydrated Zn<sup>2+</sup> ions,<sup>24</sup> La<sup>3+</sup> ions, <sup>25</sup> PANI, <sup>26</sup> structural H<sub>2</sub>O, <sup>27</sup> and so on have been reported to display high specific capacity, excellent cycling stability, and enhanced proton and Zn<sup>2+</sup> diffusion kinetics in mild RAZBs.

It is worth noting that these reports mainly focus on optimizing the effect of the preintercalated species on stabilizing layer structures to realize the enhanced reaction kinetics for protons and Zn<sup>2+</sup> ions storage. In fact, no matter how strong the pillaring effect of the preintercalated species, the phase transition from layer-type MnO<sub>2</sub> to the ZnMn<sub>2</sub>O<sub>4</sub> spinel during the longterm cycling process is inevitable due to the existence of Zn<sup>2+</sup> in the electrolyte and the Jahn-Teller Mn<sup>3+</sup>O<sub>6</sub> octahedrons.<sup>28-30</sup> Accordingly, the intrinsic role of ZnMn2O4 formation on electrode performances of manganese oxides still remains controversial. Recently, several reports have reported that some bulk ZnMn2O4 spinel forms during cycling and

Received: February 25, 2021 Accepted: April 29, 2021 Published: May 10, 2021





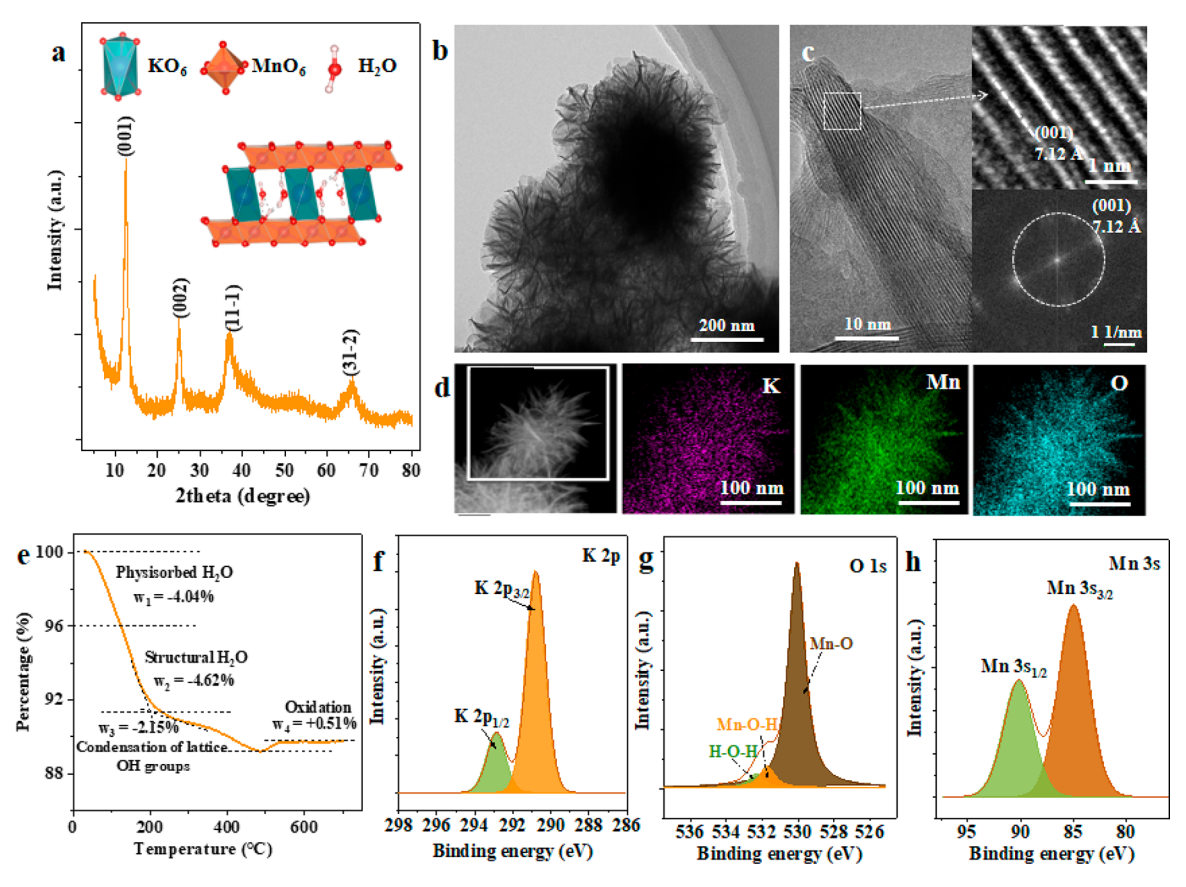


Figure 1. Material characterization of K<sub>0.36</sub>H<sub>0.26</sub>MnO<sub>2</sub>·0.28H<sub>2</sub>O (K36). (a) XRD pattern and correlated crystal structure (inset) of K36 compound. (b) TEM, (c) HRTEM morphologies, interlayer fringes, and diffraction patterns of K36, and correlated (d) EDS-mapping results of K, Mn, and O elements. (e) TGA result of K36 in O2-containing atmosphere. XPS analyses of (f) K 2p, (g) O 1s, and (h) Mn 3s peaks.

contributes to the rapid capacity fading,<sup>31,32</sup> while other reports illustrate that the electrochemically activated ZnMn2O4 spinel with nanocrystalline structure or structural defects can deliver superior electrode performances. <sup>33,34</sup> Thus, on the basis of these discussions, the role of phase transition from layer-type MnO<sub>2</sub> to the ZnMn<sub>2</sub>O<sub>4</sub> spinel still remains obscure, which blocks further advancement in the development of high-performance MnO<sub>2</sub> cathodes for next-generation aqueous batteries.

In this work, we design and synthesize high-performance  $K_{0.36}H_{0.26}MnO_2 \cdot 0.28H_2O$  (K36) as host materials in RAZBs via preintercalating protons, H2O, and K+ ions in the interlayer space of layered MnO<sub>2</sub> using a facile hydrothermal reaction and report a proton and Zn<sup>2+</sup> cointercalation mechanism in layered MnO<sub>2</sub> with the interlayer spacing remaining constant in the initial cycles. Also, we demonstrate a progressive phase evolution from layer-type K36 to hybrid layer-type K<sub>x</sub>H<sub>y</sub>Zn<sub>z</sub>MnO<sub>2</sub>·nH<sub>2</sub>O and spinel-type ZnMn<sub>2</sub>O<sub>4</sub> nanocrystals, which is responsible for the excellent electrode performances. Accordingly, K36 shows a high specific capacity (~329.8 mAh g<sup>-1</sup> at a rate current of 0.1C), a superior rate performance (~100.1 mAh g<sup>-1</sup> at a rate current of 10C), and a remarkable cycling stability (capacity retention of ~93.4% over 3000 cycles at a rate of 4C), which is among the best reported MnO2-based materials in aqueous Znion batteries. This work provides a new viewpoint on the electrochemical behavior of layered MnO2 and will be a benefit for developing more advanced rechargeable aqueous batteries.

### 2. RESULTS AND DISCUSSION

**2.1. Material Characterizations.** The K36 product with a certain amount of preintercalated hydrated protons, H<sub>2</sub>O, and K+ is synthesized using a facile hydrothermal method (the detailed synthesis process is shown in the Experimental Section. Figure 1a shows the X-ray diffraction (XRD) pattern of K36 with good crystallinity; the characteristic peaks of the (001), (002), (11-1), and (31-2) planes can be observed obviously indexing to a monoclinic birnessite phase (PDF no. 43-1317, space group C2/m).35 A transmission electron microscope (TEM) and a high-resolution transmission electron microscope (HRTEM) are applied to reveal more crystal structure features of K36. Figure 1b shows the nanoflower morphology of K36, and Figure 1c shows a well-defined lattice fringe with a clear lattice spacing of  $\sim$ 7.12 Å, corresponding well to the XRD result in Figure 1a. Besides, energy-dispersive X-ray spectroscopy (EDS)-mapping results in Figure 1d also reveal the uniform distribution of K, Mn, and O elements in K36.

It is worth noting that during synthesis some crystal water, protons, and K<sup>+</sup> ions are inevitably preintercalated into the layered MnO2, as presented in the "Analysis of Chemical Formula of Layered MnO2" section in the Supporting Information. For a general layered MnO<sub>2</sub>, the chemical formula can be expressed as  $K_xH_vMnO_2\cdot zH_2O$ , where the x, y, and z values can be modulated by tuning the reaction electrolyte compositions. The x value is directly obtained from the inductively coupled plasma optical emission spectrometer (ICP-OES) results in Table S1, and the y and z values can be obtained via calculating the thermogravimetric analysis (TGA)

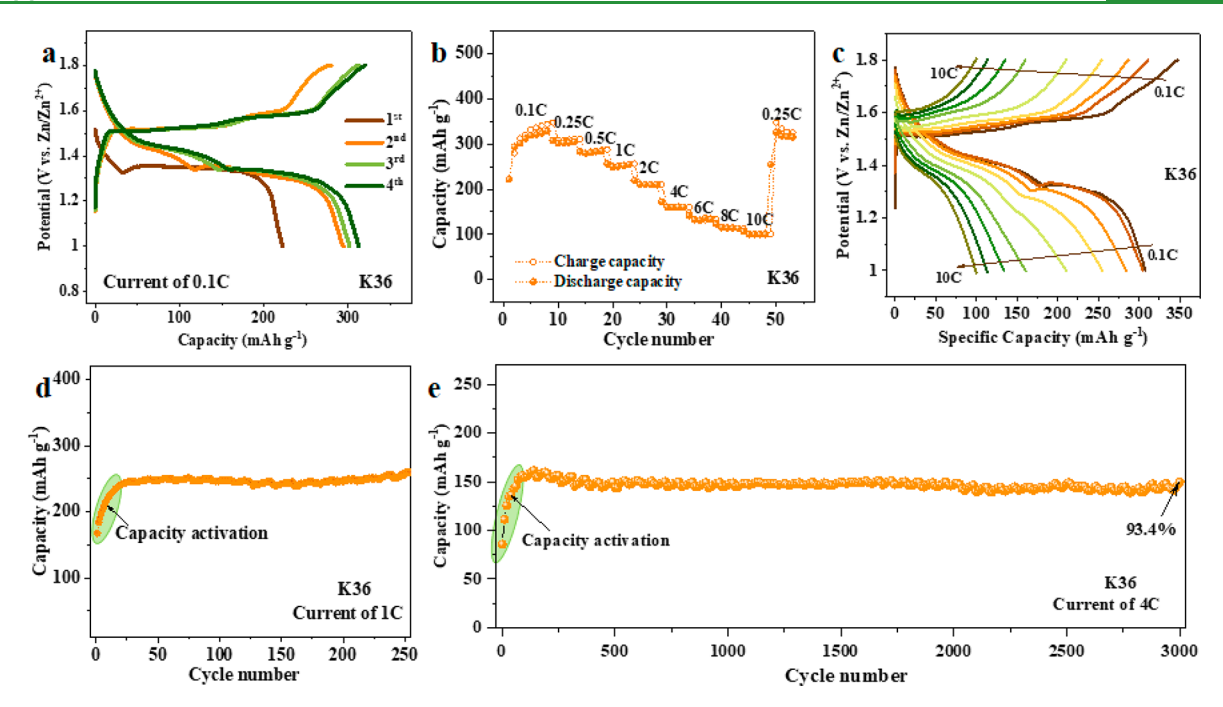


Figure 2. Electrode performances of K36 in aqueous Zn/K36 cells. (a) GCD curves of K36 electrode of the initial 4 cycles at a current of 0.1C (1C = 308 mAh g<sup>-1</sup>). (b) Rate performances of K36 electrode and (c) corresponding GCD curves at different rate currents. Cycling performances of K36 electrode at currents of (d) 1C in 250 cycles and (e) 4C in 3000 cycles.

curves in Figure 1e, in which the weight losses from  $\sim 30$  to  $\sim 100$  °C,  $\sim 100$  to  $\sim 200$  °C, and  $\sim 200$  to  $\sim 480$  °C correspond to the removal of physically absorbed water, the removal of structural water residing inside the interlayer space, and the decomposition of water by the condensation of lattice –OH groups (i.e., the preintercalated H<sup>+</sup> interacting with the lattice O of [MnO<sub>6</sub>] octahedron units), respectively. <sup>36</sup> Besides, when it further increases over  $\sim 500$  °C, the Mn<sup>2+</sup>/Mn<sup>3+</sup> oxidation of K36 in the O<sub>2</sub>-containing atmosphere leads to a certain amount of weight gain. Thus, based on these ICP-OES and TGA results, the chemical formula of K36 can be defined as  $K_{0.36}H_{0.26}MnO_2$ · 0.28 $H_2O$ .

To evidence the successful preintercalation of K<sup>+</sup> ions, protons, and structural water in K36, X-ray photoelectron spectroscopy (XPS) spectra are utilized further, in which the obvious K 2p spectra (Figure 1f) and the clear O 1s spectra consisting of Mn-O-Mn, Mn-O-H, and H-O-H peaks (Figure 1g) are observed.<sup>37</sup> Besides, for Mn 3s spectra in Figure 1h, the average oxidation state (AOS) can be calculated following the formula AOS =  $8.956 - 1.126\Delta E_{\text{Mn 3s}}^{38}$  in which the  $\Delta E_{\text{Mn 3s}}$  represents the peak splitting between the Mn  $3s_{3/2}$  and Mn  $3s_{1/2}$  peaks. It can be inferred that the AOS of Mn in K36 is calculated to be 3.40, which is consistent with the chemical formula of "K<sub>0.36</sub>H<sub>0.26</sub>MnO<sub>2</sub>·0.28H<sub>2</sub>O", verifying the rationality of the calculated chemical formula of K36 based on the ICP-OES and TGA results. The preintercalated H<sub>2</sub>O and protons can be further confirmed by Fourier transform infrared (FTIR) spectroscopy (Figure S1), in which the broad and intense adsorption peaks at ~3340 and ~1627 cm<sup>-1</sup> relate to H-OH bending vibrations and the adsorption peaks ~1110 cm<sup>-1</sup> correspond to the -OH bending vibrations combining with Mn ions in the lattice framework.

Besides, in this work, another two layer-type  $MnO_2$  are also presented as comparisons, i.e., the  $K_{0.22}H_{0.22}MnO_2\cdot 0.30H_2O$  (K22) and  $K_{0.48}H_{0.37}MnO_2\cdot 0.31H_2O$  (K48), which present similar crystal structures and morphologies but with different

amounts of preintercalated  $H_2O$ , protons, and  $K^+$  ions. The chemical formulas of K22 and K48 are obtained from the ICP-OES results in Table S1 and the TGA results in Figure S2, following the same calculation method as in the "Analysis of Chemical Formula of Layered MnO<sub>2</sub>" section in the Supporting Information. Also, the correlated XRD patterns, TEM/HRTEM/EDS-mapping results, and XPS spectra of the products are shown in Figures S3–S6.

**2.2.** Electrode Performances. To reveal the electrode performance of K36 in aqueous Zn-ion batteries, some coin-type cells are assembled and tested using K36 as the cathode, Zn foil as the anode, and aqueous 3 M ZnSO<sub>4</sub> + 0.2 M MnSO<sub>4</sub> (in water) as the electrolyte. The pre-added MnSO<sub>4</sub> in electrolyte presents little effect on the capacity delivery of K36, as evidenced in Figure S7, and its major role is to prevent the Mn<sup>3+</sup> dissolution from K36 during long-term cycling (as analyzed in the "Role of Pre-added MnSO<sub>4</sub>" section in the Supporting Information). Figure 2a shows the galvanostatic charge/discharge (GCD) curves of K36 at a current of 0.1C (1C = 308 mAh  $g^{-1}$ ). The discharge capacities are  $\sim$ 215,  $\sim$ 294,  $\sim$ 302, and  $\sim$ 313 mAh g<sup>-1</sup> in the first, second, third, and fourth cycles, respectively, indicating a gradual capacity-activation process upon cycles. The relatively lower discharge capacity in the first cycle is mainly due to the sluggish reaction kinetics for proton and Zn<sup>2+</sup> intercalation in the pristine structure of K36, as reflected in cyclic voltammetry (CV) curves (Figure S8a), in which the reduction peak value in the first cycle (~1.14 V) is much lower than that in the subsequent cycles (e.g., ~1.23 and ~1.39 V in the fourth cycle). After the first cycle, the GCD curves of K36 show two discharge platforms, which is consistent with the CV curves in Figure S8a, and have been reported referring to two kinds of proton and  $\mathrm{Zn}^{2+}$  insertion processes with different diffusion energy barriers.  $^{40,41}$  The CV curves of K22 and K48 are also provided in Figure S8b and c and demonstrate similar variation tendencies with that of K36 but with different current densities.

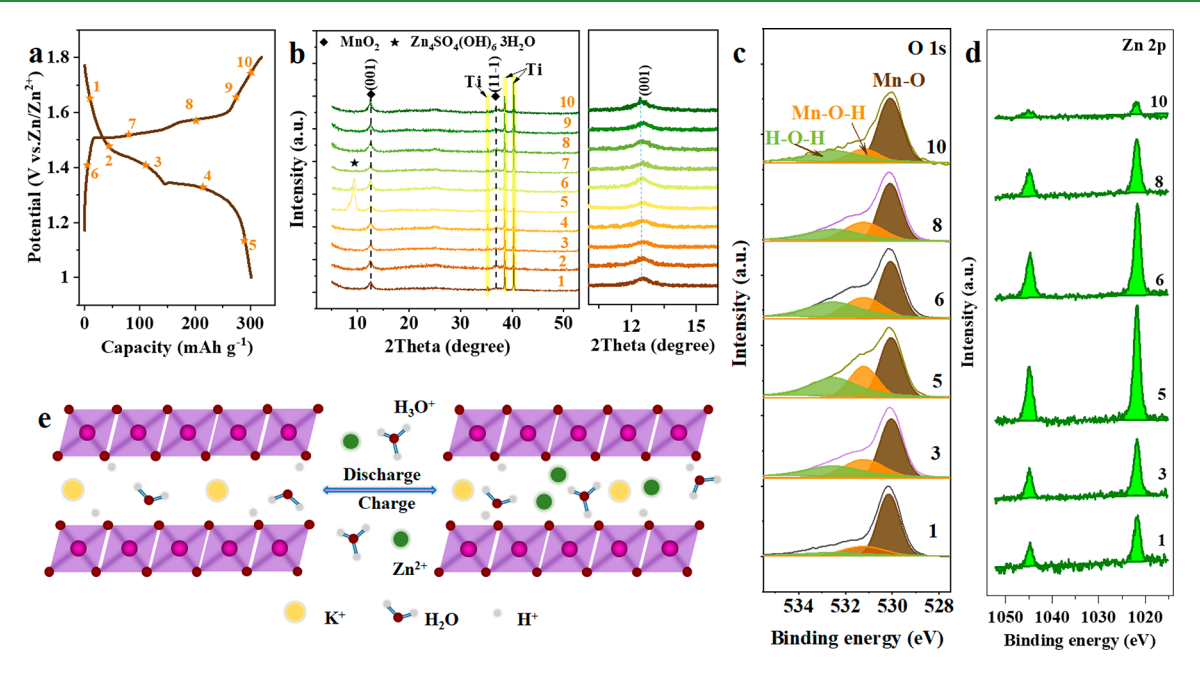


Figure 3. Proton and  $Zn^{2+}$  ions cointercalation mechanism in K36. (a) GCD curve and (b) ex situ XRD patterns at different states from point no. 1 to no. 10. XPS evolutions of (c) O 1s and (d) Zn 2p peaks of K36 electrodes upon discharge/charge process. (e) Schematic illustration of the  $H^+/Zn^{2+}$  intercalation mechanism.

Parts b and c of Figure 2 show the rate performance of K36 and the corresponding GCD curves at different rate currents, respectively. It can be seen that the K36 shows discharge capacities of 329.8, 306.7, 284.7, 252.5, 210.2, 159.6, 137.5, 115.8, and 100.2 mAh g $^{-1}$  at the increased rate currents of 0.1C, 0.25C, 0.5C, 1C, 2C, 4C, 6C, 8C, and 10C, respectively. Furthermore, when turning back to 0.25C, the discharge capacity recovers to 325.9 mAh g $^{-1}$ , demonstrating a high tolerance of K36 against massive migration of protons and Zn $^{2+}$  ions at various rate currents.

The cycling performances of K36 at rate currents of 1C and 4C are also presented in parts d and e of Figure 2, respectively. It can be seen that both cycling curves show a capacity-activation process to realize higher-capacity delivery. A phase-transition process is responsible for this capacity-activation behavior, which will be further discussed in the following part. The capacity increases from ~164 to ~249 mAh g<sup>-1</sup> in 30 cycles at a rate current of 1C and then maintains well in the subsequent cycles, showing no capacity fading in the whole 250 cycles. Meanwhile, at a rate current of 4C, the capacity increases from  $\sim$ 85 to  $\sim$ 160 mAh g<sup>-1</sup> in 150 cycles and then declines slowly in subsequent cycles, with a high capacity retention of 93.4% (compared with the highest discharge-capacity value) in 3000 cycles. These results indicate a superior cycling performance of K36. In a word, the K36 presents high capacity delivery, excellent rate performance, and superior cycling stability and is among the best reported manganese oxides in aqueous Zn-ion batteries (Table S2). As a comparison, the electrode performances of K22 and K48 are further presented and compared in Figures S9-S11, and the results indicate that K36 presents the highest capacity, rate, and cycling performances among all the electrodes, illustrating the significance of tuning the amount of preintercalated species to achieve optimized electrode performance of layer-type MnO<sub>2</sub>.

**2.3.** Proton and Zn<sup>2+</sup> Cointercalation Mechanism. Revealing the charge-storage mechanism is vital to gain insight into the intrinsic nature of the superior electrode performance of

K36. In this section, we demonstrate a proton and Zn2+ cointercalation mechanism in K36 based on a comprehensive analysis of XRD, SEM, XPS, and EDS results. Parts a and b of Figure 3 and Figure S12 show the GCD curves (in the third cycle, at a rate current of 0.1C), ex situ XRD patterns, and correlated electrode surface morphologies of K36 at various GCD states from no. 1 to no. 10, respectively. It can be seen that the characteristic peaks of the (001) planes (at 2theta =  $12.5^{\circ}$ ) of K36 remain constant during the cyclic discharge/charge processes, and some flakelike byproduct forms and disappears reversibly upon the discharge/charge processes. No other phases (e.g., MnOOH, 42 ZnMn<sub>2</sub>O<sub>4</sub>, 43 etc.) are observed in the initial cycles, and the layered structures maintain well for both the charged and discharged K36 electrode (Figure S13), indicating that the electrochemical charge storage is achieved mainly via an intercalation mechanism in the stabilized layered structure in the initial cycles rather than a conversion mechanism. Besides, we also observe the constant interlayer spacing values of the K36 electrodes during the initial cycles, which may be due to the stabilization effects of the preintercalated large-radius  $K^{\scriptscriptstyle +}$  ions, as well as the unique protons and Zn<sup>2+</sup> cointercalation mechanism, <sup>44</sup> which will be discussed in the following part.

The flakelike byproduct is well-indexed to Zn<sub>4</sub>(OH)<sub>6</sub>SO<sub>4</sub>·3H<sub>2</sub>O (PDF no. 39-0689), representing the occurrence of proton intercalation in K36 upon discharge, which has been confirmed and reported in a previous investigation.<sup>6,45,46</sup> The proton intercalation can also be identified by O 1s peaks in Figure 3c, in which the intensity of the Mn–O–H peaks (~531.5 eV) increases upon discharge and decreases upon charge, indicating a reversible intercalation/extraction of protons.<sup>7</sup> Besides, the intensity of the H–O–H peaks (~532.8 eV) also presents a similar variation tendency to that of the Mn–O–H peaks, indicating that the proton intercalation may be accompanied by some coordinated H<sub>2</sub>O. That is to say, the proton intercalation proceeds not only via H<sup>+</sup>-hopping through the Mn–O–H bonds of MnO<sub>6</sub>H<sub>x</sub> octahedronal

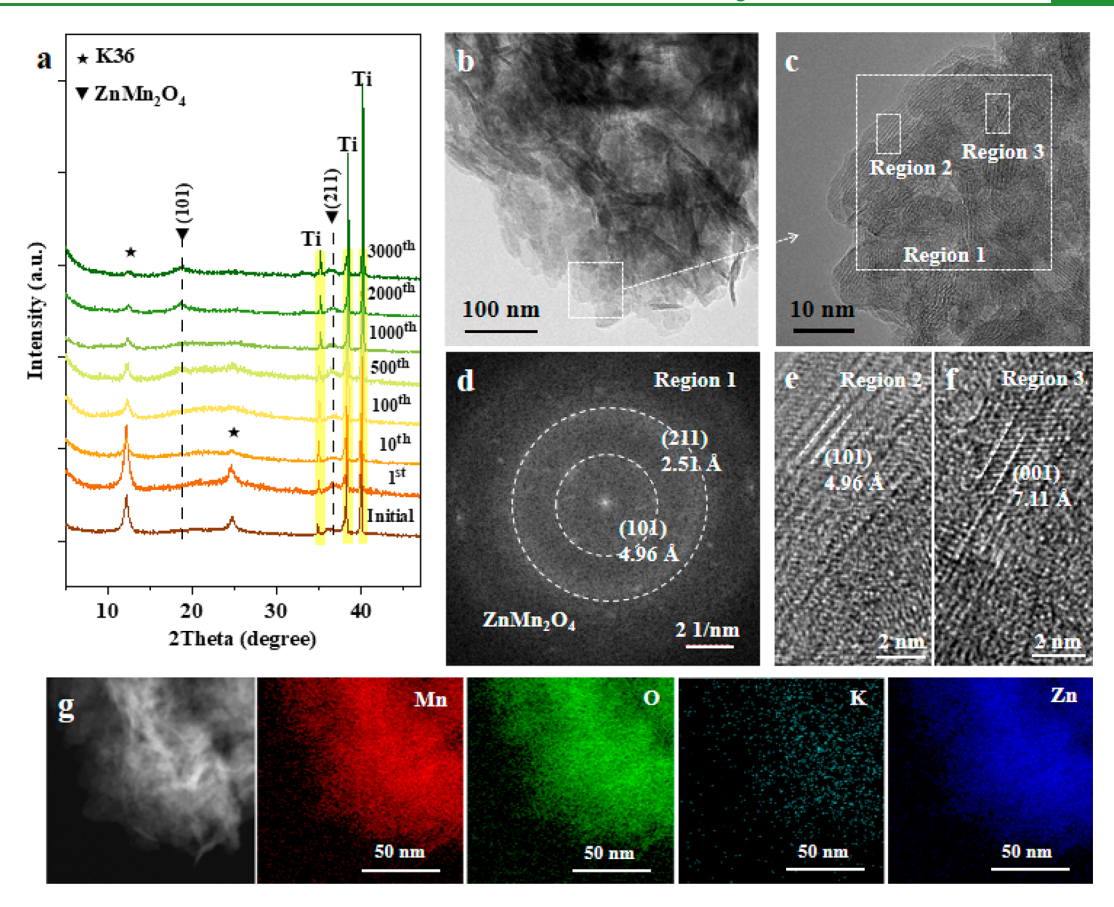


Figure 4. Progressive phase evolution during long-term cycling process. (a) Ex situ XRD patterns at fully charged state of pristine, 1st, 10th, 100th, 500th, 1000th, 2000th, and 3000th cycles at the high-rate current of 4C for K36 electrodes. (b, c) TEM and HRTEM morphologies showing the characteristic layered structure of K36 at the charged state of the 3000th cycle and (d) corresponding diffraction pattern of the  $ZnMn_2O_4$  nanocrystal (region 1 in (c)). (e, f) HRTEM morphologies of regions 2 and 3 in (c). (g) TEM and EDS-mapping results of Mn, O, K, and Zn elements for the K36 electrode after 3000 cycles (at the charged state).

structure units<sup>8</sup> but also in the form of hydronium  $(H_3O^+)$ , <sup>44,47</sup> due to the complexity of local environments in the interlayer space of layered  $MnO_2$  for proton diffusion. The cointercalation of  $H_3O$ ,  $H^+$ , and  $Zn^{2+}$  may contribute to the constant interlayer spacing of the K36 electrode in the initial cycles, similar to a previous report. <sup>44</sup> Because the precise amount of the cointercalated  $H_2O$  during discharge is difficult to measure, in this work, for simplicity, both the  $H^+$  and  $H_3O^+$  intercalations are collectively called proton intercalation. Notably, it is hard to distinguish the protons from either the electrochemically intercalated ones or the preintercalated ones, because both kinds of protons with small ion radius and low charge density can easily diffuse or transport in a hydrogen-bond network composed of Mn-O, Mn-O-H, and structural  $H_2O$  in manganese oxides.

Further, we confirm the reversible Zn<sup>2+</sup> ions intercalation/ extraction in K36 from the following three aspects. First, XPS results indicate that the intensity of the Zn 2p peaks is enhanced upon discharge and reduced upon charge, corresponding to the intercalation/extraction processes of Zn<sup>2+</sup> in K36 (Figure 3d). Second, TEM EDS-mapping results show an obvious Zn enrichment in the discharged K36 electrode, while for the charged electrode, the presence of Zn enrichment is very rare (Figure S13). Third, ICP-OES results of K36 at charged/discharged states (Table S3) also verify the successful Zn<sup>2+</sup> intercalation. Besides, the evolution of the Mn 2p and Mn 3s spectra in Figure S14 also demonstrates the decrease/increase in

chemical valence of Mn in K36 during the proton and  $Zn^{2+}$  intercalation/extraction processes. Thus, in this part, we propose a proton and  $Zn^{2+}$  intercalation mechanism that contributes greatly to the high discharge capacity and high rate performance of K36 (Figure 3e).

Besides, the electrode reaction formula of K36 is also provided, based on a comprehensive analysis combining the discharge capacity in the third cycle at 0.1C (Figure 2a), the ICP-OES results of K36 at charged/discharged states (Table S3), and the TGA results in Figure S15. A detailed calculation process is illustrated in the "Calculation Process of Electrode Reaction Formula of K36" section in the Supporting Information. It can be seen that, when discharging at a rate current of 0.1C,  $\sim$ 0.48 mol of protons and  $\sim$ 0.26 mol of Zn<sup>2+</sup> ions are intercalated into 1.00 mol of K36. The detailed electrode reaction is shown in eq 1:

$$\begin{split} &K_{0.28}Zn_{0.01}H_{0.03}MnO_2\cdot 0.18H_2O + 0.26Zn^{2+} + yH_3O^+ \\ &+ (0.48 - y)H^+ \\ &\leftrightarrow K_{0.28}Zn_{0.27}H_{0.51}MnO_2\cdot (0.18 + y)H_2O \\ &(0 < y < 0.48) \end{split} \tag{1}$$

**2.4.** Progressive Phase-Evolution Process. These results indicate a synchronous proton and  $\mathrm{Zn}^{2+}$  intercalation mechanism in K36. In this section, we reveal a progressive "layer to hybrid layer/spinel" phase-evolution process, i.e., from layer-

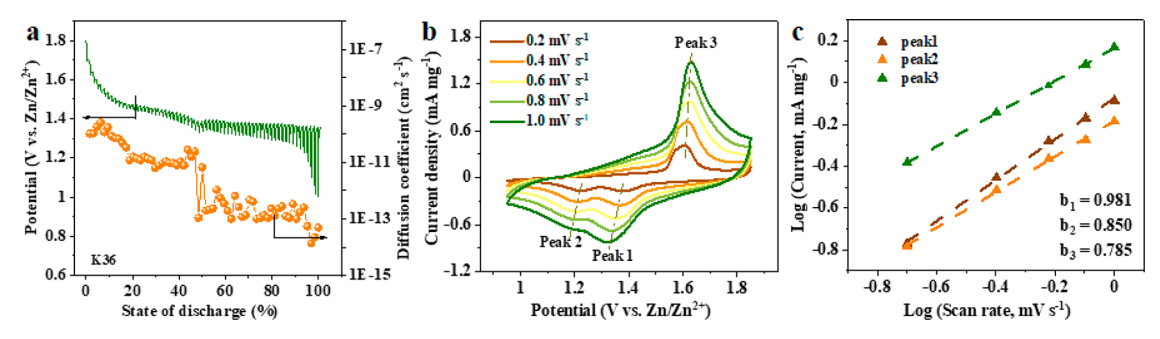


Figure 5. Electrode reaction kinetics of K36. (a) GITT curves and calculated diffusion kinetics of K36 for proton and Zn<sup>2+</sup> intercalation. (b) CV curves of K36 at scan rates from 0.2 to 1.0 mV s<sup>-1</sup> and (c) corresponding linear fittings of log(current)—log(scan rate) curves.

type K36 to hybrid layer-type K<sub>x</sub>H<sub>v</sub>Zn<sub>z</sub>MnO<sub>2</sub>·nH<sub>2</sub>O and spineltype ZnMn<sub>2</sub>O<sub>4</sub> nanocrystals, which is responsible for facile and stable proton and Zn2+ storage during long-term cycling. A phase-evolution process is revealed via a comprehensive analyses of ex situ XRD, TEM/HRTEM, and EDS-mapping results, as shown in Figure 4. When cycling at a rate current of 4C, the electrode integrity of K36 remains good in 3000 cycles (Figure S16). As illustrated in Figure 4a, the intensity of the characteristic (001) peaks (located at a 2theta of ~12.5°) of layered K36 decays gradually, while the intensity of the characteristic (101) peaks of ZnMn<sub>2</sub>O<sub>4</sub> spinel nanocrystals (located at a 2theta of ~18.7°)<sup>48</sup> increases gradually in 3000 cycles at 4C. This result provides solid evidence for the proposed progressive layer to spinel phase evolution of the K36 electrode. Meanwhile, a similar phase-evolution process is also observed in K22 and K48 electrodes (Figure S17), illustrating the universal significance of the progressive layer to hybrid layer/spinel phase evolution for layered MnO2 hosts. Despite the similar phase evolution, there exists some difference in the hybrid layer/spinel compounds after long-term cycling, indicating the regulating effect of the preintercalated K<sup>+</sup>, protons, and structural H<sub>2</sub>O to optimize the electrode performances. The discharge curves of the K36 electrode remain unchanged after 100 cycles (i.e., after the capacity-activation process), as shown in Figure S18, indicating a superior cycling stability due to this progressive layer to hybrid layer/spinel phase evolution.

This formation of ZnMn<sub>2</sub>O<sub>4</sub> nanocrystals can be further confirmed by TEM, HRTEM, and electron diffraction results. After 3000 cycles, despite the fact that the flakelike morphology of K36 is reserved to some extent (Figure 4b), the pristine feature of the layer structure of K36 (i.e., clear lattice fringes with interlayer spacing of ~7.12 Å in Figure 1c) becomes vague, as shown in Figure 4c, indicating the disappearance of a long-term ordered layer structure. The electron diffraction pattern obtained from square region 1 is shown in Figure 4d, in which two clear diffraction rings are observed, representing the (101) and (211) lattice planes of ZnMn<sub>2</sub>O<sub>4</sub> nanocrystals with interlayer spacings of ~4.96 and ~2.52 Å, respectively, 6 which is consistent with the ex situ XRD patterns of the 2000th and 3000th cycles in Figure 4a. However, no diffraction spots representing the (001) planes of K36 are observed, indicating that the ZnMn<sub>2</sub>O<sub>4</sub> nanocrystals become the main composition in the electrode after 3000 cycles. The HRTEM result in region 2 (Figure 4e) further shows a clear lattice fringe with an interlayer spacing of ~4.96 Å, related to the (101) planes of ZnMn<sub>2</sub>O<sub>4</sub> nanocrystals. The HRTEM results in region 3 (Figure 4f) show a short-term ordered lattice fringe with an interlayer spacing of ~7.10 Å, corresponding to the few-retained-layer structure of K36, which can be a type of K<sub>x</sub>H<sub>y</sub>Zn<sub>z</sub>MnO<sub>2</sub>·nH<sub>2</sub>O

layered nanodomain. Besides, TEM and EDS-mapping results (Figure 4g) also present Zn and K enrichments in the K36 electrode after 3000 cycles, where the Zn enrichment is closely related to the formation of ZnMn<sub>2</sub>O<sub>4</sub> nanocrystals, and the lower K enrichments correspond to the few-retained-layer structure of K36.

**2.5. Discussion.** Benefiting from both the proton and  $Zn^{2+}$ cointercalation mechanism and the progressive layer to spinel phase evolution, K36 presents superior reaction kinetics. The reaction kinetics for proton and Zn<sup>2+</sup> intercalations in K36 is evaluated by the galvanostatic intermittent titration technique (GITT) measurement (Figure 5a),<sup>49</sup> and the detailed calculation process is illustrated in the "Diffusion Kinetics Calculation from GITT Curves" section in the Supporting Information. The average diffusion coefficients of K36 are ~4.93  $\times~10^{-11}~\text{cm}^2~\text{s}^{-1}$  in region I (the first discharge platform in the range of  $\sim 1.65 - 1.35 \text{ V}$ ) and  $\sim 4.18 \times 10^{-13} \text{ cm}^2 \text{ s}^{-1}$  in region II (the second discharge platform in the range of  $\sim 1.35-1.15 \text{ V}$ ), which are among the best reported diffusion coefficients for manganese oxides (Table S4). Besides, compared with the GITT results of K22 and K48 (Figure S19 and Table S4), K36 shows the highest diffusion kinetics.

The superior diffusion kinetics of proton and Zn<sup>2+</sup> ions in K36 can be further identified by CV curves at scan rates from 0.2 to 1.0 mV/s (Figure 5b). The relationship between peak currents and scan rates follows the equation  $i = a \cdot v^b$ , so where *i* refers to the peak currents at different scan rates (mA mg<sup>-1</sup>), v corresponds to the scan rate (mV  $s^{-1}$ ), a and b are variable values, and the log(current)-log(scan rate) curves of K36 are linearly fitted in Figure 5c. Generally, the b value is in a range between 0.5 and 1.0; when b is close to 0.5, the solid diffusion of proton and  $Zn^{2+}$ dictates the charge/discharge process, and when b is close to 1.0, a pseudocapacitive-type diffusion kinetics is predominant. It can be observed that the b values from redox peaks 1-3 are 0.981, 0.850, and 0.785, respectively, indicating a favored capacitivetype diffusion kinetics of K36. Besides, compared with CV curves of K22 and K48 electrodes at different scan rates (Figures S20 and S21), K36 shows the highest b value, demonstrating the highest tendency of pseudocapacitive-type diffusion to promote reaction kinetics. Besides, we further notice that the proton intercalation dominates the charge-storage behavior of the K36 electrode (Figure S22 and Tables S5 and S6), illustrating an evolution from a proton and Zn<sup>2+</sup> cointercalation (in layered K36) into a proton intercalation-dominated mechanism (in layer/spinel hybrid compound), which enables the excellent cycling stability during long-term cycling.

As discussed earlier, K36 presents a high discharge capacity, an excellent rate performance, and a superior cycling stability in aqueous Zn-ion batteries. Tuning the amount of preintercalated K<sup>+</sup>, crystal water, and protons is vital to achieve optimized reaction kinetics of layered MnO<sub>2</sub>. However, because of the high complexity of the localized coordination environments in layered MnO<sub>2</sub>, the separate roles of preintercalated K<sup>+</sup> ions, crystal water, and protons are difficult to illustrate, which will be further studied in the following work. The proton and Zn<sup>2+</sup> ions cointercalation mechanism not only enables a high discharge capacity at a low rate current but also guarantees high diffusion kinetics for an excellent rate performance. Furthermore, a progressive layer to hybrid layer/spinel phase evolution (i.e., layered K36 to hybrid layer-type K<sub>x</sub>H<sub>y</sub>Zn<sub>z</sub>MnO<sub>2</sub>·nH<sub>2</sub>O and ZnMn<sub>2</sub>O<sub>4</sub> nanocrystals) during long-term cycling is demonstrated, which is closely related to the capacity-activation behavior in the initial cycles. Differing from the previous reports showing an adverse effect of ZnMn2O4 formation on the electrode performance of MnO<sub>2</sub>, for the first time, we propose that the in situ electro-induced ZnMn2O4 nanocrystals derived from a progressive layer to hybrid layer/spinel phase evolution can benefit the electrode performance of layered MnO<sub>2</sub> in an aqueous Zn-ion battery. The superior cycling performance of K36 also indicates a high structural tolerance of the electrochemically induced hybrid layer K<sub>x</sub>H<sub>y</sub>Zn<sub>z</sub>MnO<sub>2</sub>·nH<sub>2</sub>O/spinel ZnMn<sub>2</sub>O<sub>4</sub> nanocrystals against cyclic proton and Zn<sup>2+</sup> intercalation/extractions.

#### 3. CONCLUSION

In summary, we have developed a high-performance layered  $MnO_2$  ( $K_{0.36}H_{0.26}MnO_2 \cdot 0.28H_2O$ , K36) as an excellent host material in aqueous Zn-ion batteries. K36 presents a high specific capacity (~329.8 mAh g<sup>-1</sup> at 0.1C), a superior rate performance (~100.1 mAh g<sup>-1</sup> at 10C), and a remarkable cycling stability (capacity retention of ~93.4% over 3000 cycles at 4C), which are among the best reported manganese oxides in aqueous batteries. This superior electrode performance of K36 is derived from not only the proton and Zn<sup>2+</sup> cointercalation mechanism but also the progressive evolution from layer-type K36 to hybrid layer-type K<sub>x</sub>H<sub>v</sub>Zn<sub>z</sub>MnO<sub>2</sub>/spinel-type ZnMn<sub>2</sub>O<sub>4</sub> nanocrystal. This work proposes that the in situ electro-induced hybrid layer/spinel nanodomains can be high-performance host materials for cyclic proton and Zn<sup>2+</sup> intercalations/extractions, which opens a new window for developing more advanced host materials for next-generation aqueous batteries.

# 4. EXPERIMENTAL SECTION

- 4.1. Material Synthesis. In a typical hydrothermal procedure, KMnO<sub>4</sub> (7.5 mmol) and MnSO<sub>4</sub>·H<sub>2</sub>O (2.5 mmol) were dissolved in 15 mL of deionized water to form solutions A and B, respectively; then solution A was added dropwise into solution B, forming solution C. Then, 0, 5, and 10 mL of 0.1 M K<sub>2</sub>SO<sub>4</sub> solutions were added into solution C and vigorously stirred at room temperature for 20 min. The final solution was transferred into a 50 mL Teflon-lined stainless-steel autoclave for 12 h at 120 °C. The synthesized powder was collected by filtration and washed with deionized water and absolute ethanol three times, respectively. The obtained layer-type MnO<sub>2</sub> products (i.e., K22, K36, and K48) were dried at 50 °C in vacuum.
- **4.2. Material Characterization.** XRD (Bruker D8 ADVANCE) with Cu K $\alpha$  radiation was used to define the phase structure of the electrode materials. A scanning electron microscope (SEM, ZEISS SUPRA55) and transmission electron microscope (TEM, JEM-3200FS) were used to determine the micromorphology and microstructure of the products. The atomic ratios and the structural water contents of products P1-P6 were detected by inductively coupled plasma-atomic emission spectroscopy (ICP-AES, JY2000-2) and simultaneous thermal analyzer (TGA, SII STA7300 analyzer) measurements. TGA data was recorded in air using a 10 °C min<sup>-1</sup> heating rate

from room temperature to 700 °C. X-ray photoelectron spectroscopy (XPS, ESCALAB 250Xi) was used to characterize the elemental composition and electronic structure. EDS was performed using an Oxford X-Max 20.

**4.3. Electrochemical Tests.** Electrochemical performance was tested in CR2032-type coin cells assembled in air condition. The cathodes were fabricated by mixing active materials, acetylene black carbon (ABC), and polyvinylidene fluoride (PVDF) in a weight ratio of 7:2:1 with N-methyl-2-pyrrolidone (MNP) used as a solvent to form a viscous slurry and coating onto a Ti foil. The as-prepared electrodes were dried in a vacuum oven at ~110 °C for 24 h. Zinc foil (15 mm) and a glass fiber membrane were used as the anode and the separator, respectively. The active loading of manganese oxides on Ti foil was ~1.0 mg/cm<sup>2</sup>. The electrolyte contained 3 M ZnSO<sub>4</sub> and 0.2 M MnSO<sub>4</sub> in aqueous solution. The LAND-CT2001A battery-testing instrument was conducted for galvanostatically cycling with assembled cells. CV curves were carried out on a Chi 660e electrochemical workstation with a potential range from 0.95 to 1.85 V vs Zn/Zn<sup>2+</sup>.

#### ASSOCIATED CONTENT

# Supporting Information

The Supporting Information is available free of charge at https://pubs.acs.org/doi/10.1021/acsami.1c03671.

Detailed information on material synthesis procedures of MnO<sub>2</sub>, analysis of chemical formula of layered MnO<sub>2</sub>, materials characterization, and electrochemical tests (PDF)

#### AUTHOR INFORMATION

## **Corresponding Authors**

Qinghe Zhao - School of Advanced Materials, Peking University Shenzhen Graduate School, Shenzhen 518055, P. R. China; Email: zhaoqh@pku.edu.cn

Feng Pan - School of Advanced Materials, Peking University Shenzhen Graduate School, Shenzhen 518055, P. R. China; orcid.org/0000-0002-8216-1339; Email: panfeng@ pkusz.edu.cn

#### **Authors**

Shouxiang Ding - School of Advanced Materials, Peking University Shenzhen Graduate School, Shenzhen 518055, P. R. China

Lele Liu - School of Advanced Materials, Peking University Shenzhen Graduate School, Shenzhen 518055, P. R. China

Runzhi Qin - School of Advanced Materials, Peking University Shenzhen Graduate School, Shenzhen 518055, P. R. China

Xin Chen - School of Advanced Materials, Peking University Shenzhen Graduate School, Shenzhen 518055, P. R. China

Aoye Song - School of Advanced Materials, Peking University Shenzhen Graduate School, Shenzhen 518055, P. R. China

**Jiawen Li** – School of Advanced Materials, Peking University Shenzhen Graduate School, Shenzhen 518055, P. R. China

Shunning Li – School of Advanced Materials, Peking University Shenzhen Graduate School, Shenzhen 518055, P. R. China

Complete contact information is available at: https://pubs.acs.org/10.1021/acsami.1c03671

The authors declare no competing financial interest.

# ACKNOWLEDGMENTS

This work is financially supported by Basic and Applied Basic Research Foundation of Guangdong Province (no. 2019A1515110094).

### REFERENCES

- (1) Cui, Y. H.; Zhao, Q. H.; Wu, X. J.; Chen, X.; Wang, Y. T.; Qin, R. Z.; Ding, S. X.; Song, Y. L.; Wu, J. W.; Yang, K.; Wang, Z. Q.; Mei, Z. W.; Song, Z. B.; Wu, H.; Jiang, Z. Y.; Qian, G. Y.; Yang, J. L.; Yang, L. Y.; Pan, F. An Interface-Bridged Organic-Inorganic Layer that Suppresses Dendrite Formation and Side Reactions for Ultra-Long-Life Aqueous Zinc Metal Anodes. *Angew. Chem., Int. Ed.* **2020**, *59*, 16594–16601.
- (2) Wang, Z. Q.; Hu, J. T.; Han, L.; Wang, Z. J.; Wang, H. B.; Zhao, Q. H.; Liu, J. J.; Pan, F. A MOF-based Single-ion Zn<sup>2+</sup> Solid Electrolyte Leading to Dendrite-free Rechargeable Zn Batteries. *Nano Energy* **2019**, *56*, 92–99.
- (3) Qin, R. Z.; Wang, Y. T.; Zhang, M. Z.; Wang, Y.; Ding, S. X.; Song, A. Y.; Yi, H. C.; Yang, L. Y.; Song, Y. L.; Cui, Y. H.; Liu, J.; Wang, Z. Q.; Li, S. N.; Zhao, Q. H.; Pan, F. Tuning Zn<sup>2+</sup> Coordination Environment to Suppress Dendrite Formation for High-Performance Zn-ion Batteries. *Nano Energy* **2021**, *80*, 105478.
- (4) Zhao, Q. H.; Yang, J. L.; Liu, M. Q.; Wang, R.; Zhang, G. X.; Wang, H.; Tang, H. T.; Liu, C. K.; Mei, Z. W.; Chen, H. B.; Pan, F. Tuning Electronic Push/Pull of Ni-Based Hydroxides To Enhance Hydrogen and Oxygen Evolution Reactions for Water Splitting. *ACS Catal.* **2018**, *8*, 5621–5629.
- (5) Qin, R. Z.; Wang, Y.; Zhao, Q. H.; Yang, K.; Pan, F. EQCM for Indepth Study of Metal Anodes for Electrochemical Energy Storage. *Chin. J. Struct. Chem.* **2020**, *39*, 605–614.
- (6) Liu, M. Q.; Zhao, Q. H.; Liu, H.; Yang, J. L.; Chen, X.; Yang, L. Y.; Cui, Y. H.; Huang, W. Y.; Zhao, W. G.; Song, A. Y.; Wang, Y. T.; Ding, S. X.; Song, Y. L.; Qian, G. Y.; Chen, H. B.; Pan, F. Tuning Phase Evolution of β-MnO<sub>2</sub> during Microwave Hydrothermal Synthesis for High-Performance Aqueous Zn Ion Battery. *Nano Energy* **2019**, *64*, 103942.
- (7) Zhao, Q. H.; Chen, X.; Wang, Z. Q.; Yang, L. Y.; Qin, Y. Z.; Yang, J. L.; Song, Y. L.; Ding, S. X.; Weng, M. Y.; Huang, W. Y.; Liu, J. J.; Zhao, W. G.; Qian, G. Y.; Yang, K.; Cui, Y. H.; Chen, H.; Pan, F. Unravelling H<sup>+</sup>/Zn<sup>2+</sup> Synergistic Intercalation in a Novel Phase of Manganese Oxide for High-Performance Aqueous Rechargeable Battery. *Small* **2019**, *15*, 1904545.
- (8) Zhao, Q. H.; Song, A. Y.; Zhao, W. G.; Qin, Y. Z.; Ding, S. X.; Chen, X.; Song, Y. L.; Yang, L. Y.; Lin, H.; Li, S. N.; Pan, F. Boosting the Energy Density of Aqueous Batteries via Facile Grotthuss Proton Transport. *Angew. Chem., Int. Ed.* **2021**, *60*, 4169–4174.
- (9) Yi, H. C.; Qin, R. Z.; Ding, S. X.; Wang, Y. T.; Li, S. N.; Zhao, Q. H.; Pan, F. Structure and Properties of Prussian Blue Analogues in Energy Storage and Conversion Applications. *Adv. Funct. Mater.* **2021**, 31, 2006970.
- (10) Ma, L. T.; Chen, S. M.; Long, C. B.; Li, X. L.; Zhao, Y. W.; Liu, X. X.; Huang, Z. D.; Dong, B. B.; Zapien, J. A.; Zhi, C. Y. Achieving High-Voltage and High-Capacity Aqueous Rechargeable Zinc Ion Battery by Incorporating Two-Species Redox Reaction. *Adv. Energy Mater.* **2019**, 9, 1902446.
- (11) Lu, Y. Y.; Zhu, T. Y.; van den Bergh, W.; Stefik, M.; Huang, K. A High Performing Zn-Ion Battery Cathode Enabled by In Situ Transformation of  $V_2O_5$  Atomic Layers. *Angew. Chem., Int. Ed.* **2020**, 59, 17004–17011.
- (12) Wan, F.; Niu, Z. Design Strategies for Vanadium-based Aqueous Zinc-Ion Batteries. *Angew. Chem., Int. Ed.* **2019**, *58*, 16358–16367.
- (13) Huang, S.; Wan, F.; Bi, S. S.; Zhu, J. C.; Niu, Z. Q.; Chen, J. A Self-Healing Integrated All-in-One Zinc-Ion Battery. *Angew. Chem.* **2019**, 131, 4357–4361.
- (14) Tie, Z. W.; Liu, L. J.; Deng, S. Z.; Zhao, D. B.; Niu, Z. Q. Proton Insertion Chemistry of Zn/Organic Battery. *Angew. Chem.* **2020**, *132*, 4950–4954.
- (15) Gao, X.; Wu, H. W.; Li, W. J.; Tian, Y.; Zhang, Y.; Wu, H.; Yang, L.; Zou, G. Q.; Hou, H. S.; Ji, X. B.  $H^+$ -Insertion Boosted  $\alpha$ -MnO<sub>2</sub> for an Aqueous Zn-Ion Battery. *Small* **2020**, *16*, 1905842.
- (16) Li, L. Y.; Hoang, T. K. A.; Zhi, J.; Han, M.; Li, S. K.; Chen, P. Functioning Mechanism of the Secondary Aqueous Zn-β-MnO<sub>2</sub> Battery. *ACS Appl. Mater. Interfaces* **2020**, *12*, 12834–12846.
- (17) Wang, C.; Zeng, Y. X.; Xiao, X.; Wu, S. J.; Zhong, G. B.; Xu, K. Q.; Wei, Z. F.; Su, W.; Lu, X. H. γ-MnO<sub>2</sub> Nanorods/Graphene Composite

- as Efficient Cathode for Advanced Rechargeable Aqueous Zinc-ion Battery. *J. Energy Chem.* **2020**, 43, 182–187.
- (18) Xiong, T.; Yu, Z. G.; Wu, H. J.; Du, Y. H.; Xie, Q. D.; Chen, J. S.; Zhang, Y.-W.; Pennycook, S. J.; Lee, W. S. V.; Xue, J. M. Defect Engineering of Oxygen-Deficient Manganese Oxide to Achieve High-Performing Aqueous Zinc Ion Battery. *Adv. Energy Mater.* **2019**, *9*, 1803815.
- (19) Jiang, H.; Wei, Z. X.; Ma, L.; Yuan, Y. F.; Hong, J. J.; Wu, X. Y.; Leonard, D. P.; Holoubek, J.; Razink, J.; Stickle, W. F.; Du, F.; Wu, T. P.; Lu, J.; Ji, X. L. An Aqueous Dual-Ion Battery Cathode of Mn<sub>3</sub>O<sub>4</sub> via Reversible Insertion of Nitrate. *Angew. Chem.* **2019**, *131*, 5340–5345.
- (20) Song, Y.; Pan, Q.; Lv, H.; Yang, D.; Qin, Z.; Zhang, M.-Y.; Sun, Q.; Liu, X.-X. Ammonium-Ion Storage Using Electrodeposited Manganese Oxides. *Angew. Chem., Int. Ed.* **2021**, *60*, 5718–5722.
- (21) Li, W.; Han, C.; Wang, Y.; Liu, H.-K. Structural Modulation of Manganese Oxides for Zinc-ion Batteries. *Chin. J. Struct. Chem.* **2020**, 39, 31–35.
- (22) Zhao, Q. H.; Ding, S. X.; Song, A. Y.; Qin, R. Z.; Pan, F. Tuning Structure of Manganese Oxides to Achieve High-Performance Aqueous Zn Batteries. *J. Struct. Chem.* **2020**, *39*, 388–394.
- (23) Zhao, Q. H.; Song, A. Y.; Ding, S. X.; Qin, R. Z.; Cui, Y. H.; Li, S. N.; Pan, F. Pre-Intercalation Strategy in Manganese Oxides for Electrochemical Energy Storage: Review and Prospect. *Adv. Mater.* **2020**, *32*, 2002450.
- (24) Wang, J. J.; Wang, J.-G.; Liu, H. Y.; Wei, C. G.; Kang, F. Y. Zinc ion Stabilized MnO<sub>2</sub> Nanospheres for High Capacity and Long Lifespan Aqueous Zinc-ion Batteries. *J. Mater. Chem. A* **2019**, *7*, 13727.
- (25) Zhang, H. Z.; Liu, Q. Y.; Wang, J.; Chen, K. F.; Xue, D. F.; Liu, J.; Lu, X. H. Boosting the Zn-ion Storage Capability of Birnessite Manganese Oxide Nano-florets by La<sup>3+</sup> Intercalation. *J. Mater. Chem. A* **2019**, *7*, 22079–22083.
- (26) Huang, J. H.; Wang, Z.; Hou, M. Y.; Dong, X. L.; Liu, Y.; Wang, Y. G.; Xia, Y. Y. Polyaniline-Intercalated Manganese Dioxide Nanolayers as a High-Performance Cathode material for an Aqueous Zinc-ion Battery. *Nat. Commun.* **2018**, *9*, 2906.
- (27) Nam, K. W.; Kim, H. J.; Choi, J. H.; Choi, J. W. Crystal Water for High Performance Layered Manganese Oxide Cathodes in Aqueous Rechargeable Zinc Batteries. *Energy Environ. Sci.* **2019**, *12*, 1999.
- (28) Alfaruqi, M. H.; Islam, S.; Putro, D. Y.; Mathew, V.; Kim, S.; Jo, J.; Kim, S.; Sun, Y.; Kim, Y.; Kim, K. Structural Transformation and Electrochemical Study of Layered MnO<sub>2</sub> in Rechargeable Aqueous Zinc-ion Battery. *Electrochim. Acta* **2018**, 276, 1–11.
- (29) Zhao, S.; Han, B.; Zhang, D. T.; Huang, Q.; Xiao, L.; Chen, L. B.; Ivey, D. G.; Deng, Y. D.; Wei, W. F. Unravelling the Reaction Chemistry and Degradation Mechanism in Aqueous Zn/MnO<sub>2</sub> Rechargeable Batteries. *J. Mater. Chem. A* **2018**, *6*, 5733–5739.
- (30) Huang, Y. F.; Mou, J.; Liu, W. B.; Wang, X. L.; Dong, L. B.; Kang, F. Y.; Xu, C. J. Novel Insights into Energy Storage Mechanism of Aqueous Rechargeable  $Zn/MnO_2$  Batteries with Participation of  $Mn^{2+}$ . *Nano-Micro Lett.* **2019**, *11*, 49.
- (31) Alfaruqi, M. H.; Gim, J.; Kim, S.; Song, J. J.; Pham, D. T.; Jo, J.; Xiu, Z. L.; Mathew, V.; Kim, J. A Layered  $\delta$ -MnO<sub>2</sub> Nanoflake Cathode with High Zinc-Storage Capacities for Eco-friendly Battery applications. *Electrochem. Commun.* **2015**, *60*, 121–125.
- (32) Li, Y.; Wang, S. Y.; Salvador, J. R.; Wu, J. P.; Liu, B.; Yang, W. L.; Yang, J.; Zhang, W. Q.; Liu, J.; Yang, J. H. Reaction Mechanisms for Long-Life Rechargeable Zn/MnO<sub>2</sub> Batteries. *Chem. Mater.* **2019**, *31*, 2036–2047.
- (33) Zhang, H. Z.; Wang, J.; Liu, Q. Y.; He, W. Y.; Lai, Z. Z.; Zhang, X. Y.; Yu, M. H.; Tong, Y. X.; Lu, X. H. Extracting oxygen anions from ZnMn<sub>2</sub>O<sub>4</sub>: Robust Cathode for Flexible All-Solid-State Zn-ion Batteries. *Energy Storage Mater.* **2019**, *21*, 154–161.
- (34) Yang, S. N.; Zhang, M. S.; Wu, X. W.; Wu, X. S.; Zeng, F. H.; Li, Y. T.; Duan, S. Y.; Fan, D. H.; Yang, Y.; Wu, X. M. The Excellent Electrochemical Performances of ZnMn<sub>2</sub>O<sub>4</sub>/Mn<sub>2</sub>O<sub>3</sub>: The Composite Cathode Material for Potential Aqueous Zinc Ion Batteries. *J. Electroanal. Chem.* **2019**, 832, 69–74.
- (35) Guo, C.; Liu, H. M.; Li, J. F.; Hou, Z. G.; Liang, J. W.; Zhou, J.; Zhu, Y. C.; Qian, Y. T. Ultrathin  $\delta$ -MnO $_2$  Nanosheets as Cathode for

- Aqueous Rechargeable Zinc Ion Battery. *Electrochim. Acta* **2019**, 304, 370–377.
- (36) Lv, D. P.; Huang, X. K.; Yue, H. J.; Yang, Y. Sodium-Ion-Assisted Hydrothermal Synthesis of  $\gamma$ -MnO<sub>2</sub> and Its Electrochemical Performance. *J. Electrochem. Soc.* **2009**, *156*, A911—A916.
- (37) Liu, G. X.; Huang, H. W.; Bi, R.; Xiao, X.; Ma, T. Y.; Zhang, L. K<sup>+</sup> Pre-intercalated Manganese Dioxide with Enhanced Zn<sup>2+</sup> Diffusion for High Rate and Durable Aqueous Zinc-ion Battery. *J. Mater. Chem. A* **2019**, *7*, 20806–20812.
- (38) Poyraz, A.; Laughlin, J.; Zec, Z. Improving the Cycle Life of Cryptomelane type Manganese Dioxides in Aqueous Rechargeable Zinc Ion Batteries: The effect of electrolyte concentration. *Electrochim. Acta* **2019**, *305*, 423–432.
- (39) Dubal, D. P.; Lokhande, C. D. Significant Improvement in the Electrochemical Performances of Nano-nest like Amorphous  $MnO_2$  Electrodes due to Fe Doping. *Ceram. Int.* **2013**, 39, 415–423.
- (40) Sun, T. J.; Nian, Q. S.; Zheng, S. B.; Shi, J. Q.; Tao, Z. L. Layered Ca<sub>0.28</sub>MnO<sub>2</sub>·0.5H<sub>2</sub>O as a High-Performance Cathode for Aqueous Zinc-Ion Battery. *Small* **2020**, *16*, 2000597.
- (41) Zhang, X. Y.; Wu, S. W.; Deng, S. J.; Wu, W. X.; Zeng, Y. X.; Xia, X. H.; Pan, G. X.; Tong, Y. X.; Lu, X. H. 3D CNTs Networks Enable MnO<sub>2</sub> Cathodes with High Capacity and Superior Rate Capability for Flexible Rechargeable Zn-MnO<sub>2</sub> Batteries. *Small Methods* **2019**, 3, 1900525.
- (42) Pan, H. L.; Shao, Y. Y.; Yan, P. F.; Cheng, Y. W.; Han, K. S.; Nie, Z. M.; Wang, C. M.; Yang, J. H.; Li, X. L.; Bhattacharya, P.; Mueller, K. T.; Liu, J. Reversible Aqueous Zinc/Manganese Oxide Energy Storage from Conversion Reactions. *Nat. Energy* **2016**, *1*, 16039.
- (43) Yang, J.; Cao, J. Y.; Peng, Y. D.; Yang, W. J.; Barg, s.; Liu, Z.; Kinloch, L.; Bissett, M. A.; Dryfe, R. A. W. Unravelling the Mechanism of Rechargeable Aqueous Zn-MnO<sub>2</sub> Batteries: Implementation of Charging Process by Electrodeposition of MnO<sub>2</sub>. *ChemSusChem* **2020**, *13*, 4103–4110.
- (44) Wang, L. L.; Huang, K.-W.; Chen, J. T.; Zheng, J. R. Ultralong Cycle Stability of Aqueous Zinc-ion Batteries with Zinc Vanadium Oxide Cathodes. *Sci. Adv.* **2019**, *5*, eaax4279.
- (45) Zhao, Q.; Huang, J.; Zhou, M. M.; Ju, Z. N.; Sun, X. D.; Sun, Y.; Huang, Z. H.; Li, H.; Ma, T. Y. Proton Insertion Promoted a Polyfurfural/MnO<sub>2</sub> Nanocomposite Cathode for a Rechargeable Aqueous Zn-MnO<sub>2</sub> Battery. ACS Appl. Mater. Interfaces 2020, 12, 36072—36081.
- (46) Dong, Y.; Jia, M.; Wang, Y. Y.; Xu, J. Z.; Liu, Y. C.; Jiao, L. F.; Zhang, N. Long-Life Zinc/Vanadium Pentoxide Battery Enabled by a Concentrated Aqueous ZnSO<sub>4</sub> Electrolyte with Proton and Zinc Ion Co-Intercalation. *ACS Appl. Energy Mater.* **2020**, *3*, 11183–11192.
- (47) Zhang, H. Z.; Wu, W. X.; Liu, Q. Y.; Yang, F.; Shi, X.; Liu, X. Q.; Yu, M. H.; Lu, X. H. Interlayer Engineering of α-MoO<sub>3</sub> Modulates Selective Hydronium Intercalation in Neutral Aqueous Electrolyte. *Angew. Chem., Int. Ed.* **2021**, *60*, 896–903.
- (48) Zhang, N.; Cheng, F. Y.; Liu, Y. C.; Zhao, Q.; Lei, K. X.; Chen, C. C.; Liu, X. S.; Chen, J. Cation-Deficient Spinel  $ZnMn_2O_4$  Cathode in  $Zn(CF_3SO_3)_2$  Electrolyte for Rechargeable Aqueous Zn-Ion Battery. *J. Am. Chem. Soc.* **2016**, 138, 12894.
- (49) Yuan, Y. F.; Zhan, C.; He, K.; Chen, H. R.; Yao, W. T.; Sharifi-Asl, S.; Song, B. A.; Yang, Z. Z.; Nie, A. M.; Luo, X. Y.; Wang, H.; Wood, S. M.; Amine, K.; Islam, M. S.; Lu, J.; Shahbazian-Yassar, R. The influence of large cations on the electrochemical properties of tunnel-structured metal oxides. *Nat. Commun.* **2016**, *7*, 13374.
- (50) Zhang, Y.; Deng, S. J.; Luo, M.; Pan, G. x.; Zeng, Y. X.; Lu, X. H.; Ai, C. Z.; Liu, Q.; Xiong, Q. Q.; Wang, X. L.; Xia, X. H.; Tu, J. P. Defect Promoted Capacity and Durability of N-MnO<sub>2-x</sub> Branch Arrays via Low-Temperature NH<sub>3</sub> Treatment for Advanced Aqueous Zinc Ion Batteries. *Small* **2019**, *15*, 1905452.